Journal of
Materials in Life Sciences

Vol. 3 No. 1 (2024)

Full Paper

Cobalt Doped Tin (IV) Oxide Nanorods: A Potential Ethanol Gas Sensor

Vicinisvarri Inderan[a,b], Hooi ling Lee[a,*], Norain Isa [b], Wan Zuraida Wan Kamis[b]

[a] Nanomaterials Research Group, School of Chemical Sciences, Universiti Sains Malaysia, 11800 USM, Penang, Malaysia.
[b] Chemical Engineering Studies, College of Engineering, Universiti Teknologi MARA, Penang Branch, Permatang Pauh campus, Malaysia.

Article history
Received
14 September 2023
Revised
10 April 2024
Accepted
23 April 2024
Published online
30 May 2024

*Corresponding author
hllee@usm.my

Abstract

The introduction of transitional metals into metal oxide matrices can lead to synergistic physiochemical properties compared to the pristine components, offering significant potential across various applications such as gas sensors, photocatalysts and energy storage. This study focuses on hydrothermal synthesis of cobalt-doped tin (IV) oxide (Co:SnO_2) nanorods with different Co doping dosages ranging from 0.5–5 mol%. To investigate the physiochemical properties of the as-synthesized Co:SnO_2, samples were analyzed by X-ray diffraction (XRD), high-resolution transmission electron microscopy with selected area electron diffraction (HRTEM/SAED) and X-ray photoelectron spectroscopy (XPS). The findings reveal that the Co dopant did not noticeably change the shape of SnO_2 nanorods. Nevertheless, the size of the nanorods decreased, which is a common behavior observed with transition metal dopants. To study the sensing performance, the undoped SnO_2 and 5Co:SnO_2 nanorod samples were tested on 1000 ppm ethanol gas and N_2 carrier gas at 450°C, the optimum operation temperature. The result indicates that the sensing response of 5Co:SnO_2 nanorods recorded 3 times higher response, R_0/R_g, 3300 compared to the undoped SnO_2 nanorods sensor R_0/R_g, 1100. This study suggests that the improvement in ethanol gas sensing performance can be attributed to the changes in physicochemical properties, such as particle size reduction, band gap narrowing, and the presence of oxygen vacancies.

Keywords Co-doped, tin (IV) oxide, nanorods, ethanol gas sensor, hydrothermal

1.0 INTRODUCTION

The exploitation of metal oxides in gas sensors has become increasingly prominent among researchers ever since Seiyama and colleagues demonstrated that the electric conductivity of zinc oxide (ZnO) film changed rapidly upon adsorption and desorption of gases on the surface of ZnO. Since then, numerous types of metal oxides have been intensively studied for gas-sensing applications [1]. Among these, one-dimensional (1-D) metal oxide nanostructures have emerged as promising candidates for gas sensors, primarily because of their exceptionally high surface-to-volume ratio, which leads to enhanced sensor performance. Various types of 1-D metal oxide nanostructures, such as nanowires, nanotubes, nanospheres, nanorods, and nanobelts, have been synthesized and investigated for their potential in gas sensing applications [2, 3].

Tin oxide (SnO_2) is one of the first and most extensively used sensing materials in gas sensor devices due to its unique characteristics, including a broad band gap (3.6 eV at 300 K), a large exciton binding energy (130 meV), and high electron mobility (100–200 cm^2 Ve^{-1} S^{-1}) [4].

Typically, the physiochemical properties of SnO_2 are determined by the specific synthesis method chosen. The production of 1-D SnO_2 has been accomplished *via* several methods, including sol-gel, thermal evaporation, hydrothermal,

chemical vapor deposition (CVD) [5] and co-precipitation. Among these methods, the hydrothermal approach has been widely used to fabricate homogeneous SnO_2 nanostructures with well-controlled shapes and sizes. The hydrothermal method involves the formation and growth of nanocrystals *via* a chemical reaction that occurs within a sealed, heated aqueous solution under high temperature and pressure [6].

Despite 1-D SnO_2 nanostructures showing encouraging results in gas sensor applications, enhancing their gas sensing response and recovery time and lowering the operating temperature remain significant challenges. Therefore, considerable work has been dedicated to improving SnO_2-based gas sensors [3].

Previous studies revealed that doping with noble metals or transition metals could enhance the overall sensing properties of SnO_2 nanostructures. Noble metal dopants, for instance, Pd and Pt, have been widely recognized for their great improvement in gas-sensing properties [7]. However, their high cost constrained actual usage [8]. Therefore, exploring more cost-effective alternatives, such as common *3d* transition metals, is crucial.

The current research focuses on the hydrothermal synthesis of cobalt (Co) doped SnO_2 nanorods and evaluates the effect of the doping dosage on the morphological and structural characteristics of SnO_2 nanorods. The SnO_2 nanorod samples were then tested on ethanol gas to correlate the characteristics of the sensor material with the ethanol sensor response. Ethanol gas sensors are widely used in producing biofuels and pharmaceuticals, particularly during fermentation. It is essential to monitor the concentration of ethanol gas during the fermentation reaction, ensuring optimal conditions for the growth of microorganisms [9].

2.0 EXPERIMENTAL

2.1 Materials

All chemicals used in this study were of analytical grade without further purification. Tin(IV) chloride pentahydrate, $SnCl_4 \cdot 5H_2O$ (98%) (molecular weight (MW = 350.58 g mol^{-1}) was obtained from Sigma-Aldrich. Sodium hydroxide (NaOH) (MW = 39.99 g mol^{-1}) pellets, absolute ethanol (C_2H_5OH) (MW = 46.07 g mol^{-1}), cobalt(II) chloride 97% anhydrous, $CoCl_2$ (MW= 129.84 g mol^{-1}) were procured from Hamburg Chemical GmbH. Gases such as HiQ nitrogen 5.0 (99.9%) and HiQ argon 5.0 (99.9%) and 1000 ppm ethanol/N_2 for gas sensing tests were supplied by Linde Malaysia Sdn. Bhd.

2.2 Synthesis of Co-doped SnO_2

A detailed description of the hydrothermal synthesis of SnO_2 and doped SnO_2 nanorods may be found in our earlier publications [10-12]. In brief, the reaction solution was prepared by dissolving 4.8 mmol tin tetrachloride pentahydrate ($SnCl_4.5H_2O$) salt and a desired amount of $CoCl_2$ (0.5, 1, 3 and 5 mol%) in 30 ml of solvent, which consisted of a 1:1 v/v mixture of absolute ethanol-distilled water. While stirring, 6 M sodium hydroxide aqueous solution (NaOH) was added dropwise to adjust the pH of the reaction solution to pH 13. In order to balance the ratio of absolute ethanol to distilled water, an equal amount of absolute ethanol was added to the reaction mixture. A light orange color suspension was obtained, which was later transferred into a 50 ml Teflon-lined stainless-steel autoclave, sealed and heated to 180 °C for 15 hours. After cooling, the obtained precipitates were centrifuged and washed with distilled water and ethanol at 750 rpm. Finally, the wet precipitates were dried in an oven at 55 °C for 24 hours. The undoped SnO_2 nanorod powder sample was synthesized following the same procedure as above, except the heat-treatment duration was extended to 24 hours without $CoCl_2$.

2.3 Characterization

The crystal structure of the samples was analyzed using X-ray diffraction (XRD, PW 3040/60 X'PERT PRO (PANalytical), which was equipped with Cu Kα radiation. The scanning was done with a step size of 0.0340°. The band gap energies were obtained using an Ultraviolet–Visible spectrometer (UV-Vis) (Perkin Elmer Lambda 35, United States) at a wavelength range of 200–600 nm. The surface composition analysis was performed using X-ray photoelectron spectroscopy (XPS) (Axia Ultra DLDXPS, Kratos) with a monochromatic Al Kα X-ray source (1486.6 eV of photons) and a background pressure of 10^{-7} Pa. The binding energy (BE) data recorded by XPS were corrected using the C 1s peak at 284.6 eV, and all the XPS data was processed using CASAXPS (version 2.3.17) software. A GL (30) Gaussian (70%)-Lorentzian (30%) profile and a standard Shirley background were applied for fitting the components in order to reduce the least square error of the fit. The morphologies of the samples were investigated by high-resolution transmission electron microscopy (HRTEM) TECNAI G2 20 S-TWIN, FEI) at 200 kV.

2.4 Ethanol gas sensing measurement

The ethanol gas sensing test was conducted using custom-built gas sensing measurement instrumentation. The set-up diagram can be referenced in our previous work [10]. Prior to the test, the selected powder samples (SnO_2 and $5Co:SnO_2$) were mixed with sensor ink to form a slurry, which was then coated onto Au-interdigitated alumina substrates (5 mm × 5 mm) (Case Western Reserve University, Cleveland, United States). The sample coated substrates were stabilized at 450°C in argon gas flow for approximately one hour. Then, 1000 ppm ethanol gas with nitrogen as a carrier gas was passed through the sensor at a flow rate of 200 sccm. The electrical resistance of the sensor was measured at a temperature of 450 °C, which was determined to be the optimum operating temperature [10]. In this study, the sensor sensitivity was defined as $(R_0–R_g)/R_g$, where R_0 represents the resistance of the sensor material in nitrogen gas, and R_g represents the resistance of the sensor material in ethanol gas. The response time refers to the time required for the sensor to reach 90% of the total resistance changes after introducing the target gas. Conversely, the recovery time is defined as the duration taken by the sensor to attain 90% of total resistance changes upon removing ethanol gas [11].

3.0 RESULTS AND DISCUSSION

3.1 Characterization of SnO_2

3.1.1 X-ray Diffraction

The effect of different dosages of Co doping on the crystallographic properties of SnO_2 was studied using XRD analysis. Figure 1 illustrates the XRD patterns of the samples. All diffraction peaks observed for the undoped SnO_2 and Co-doped SnO_2 samples can be indexed to the rutile tetragonal crystal structure (ICSD 092552). In addition, the absence of secondary phases such as metallic Co and cobalt oxide (CoO or Co_2O_3) peaks, suggesting substitutions of Co in the Sn-site [12]. There are three main peaks around 2θ values of 26º, 33º and 51º, corresponding to (110), (110) and (211) planes, indicating that the preferential crystal plane remained unchanged (101) despite the rise in Co dopant dosage.

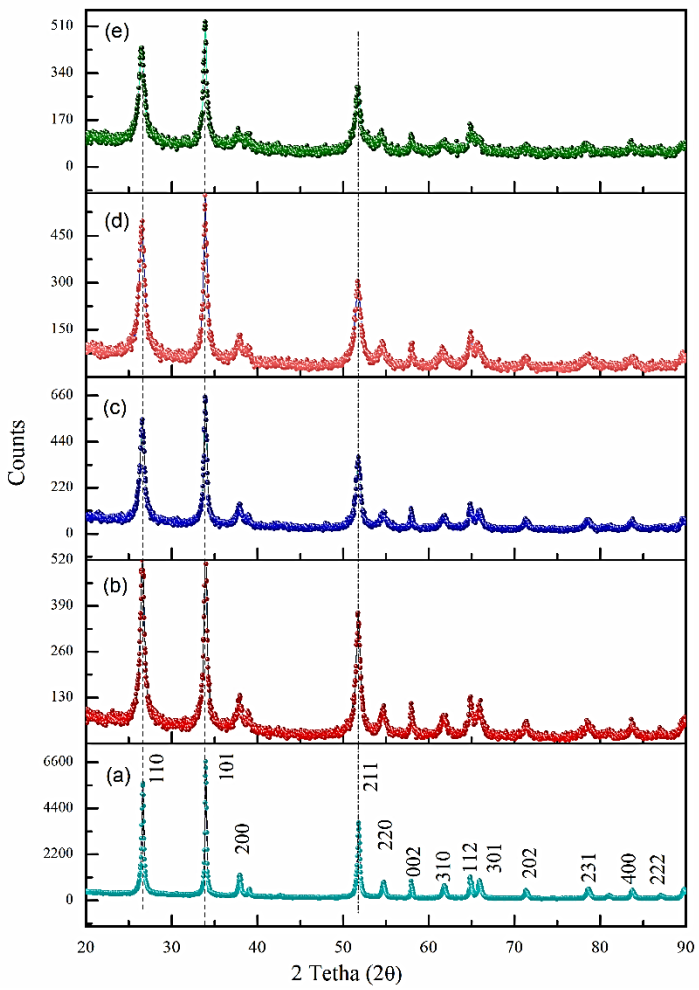

Figure 1 XRD patterns of SnO_2 samples as follows (a) SnO_2, (b) 0.5Co:SnO_2, (c) 1Co:SnO_2 and (d) 3Co:SnO_2 and (e) 5Co:SnO_2.

The XRD results were further analyzed by calculating the crystallographic parameters, and the data are presented in Table 1. The crystallite size was determined by employing the Scherrer formula, as expressed in equation (1).

$$D = \frac{K\lambda}{\beta \cos\theta} \quad (1)$$

where *D* is the average crystallite size, *K* is a constant typically assigned a value of 0.9, associated with crystallite shape, β indicates the full width at half of peak maximum (FWHM), and *θ* represents the Bragg's angle. By using the value of *d*, it is possible to calculate the lattice parameters, *a* and *c* of rutile tetragonal using the following relation (2):

$$\frac{1}{d^2} = \frac{h^2+k^2}{a^2} + \frac{l^2}{c^2} \quad (2)$$

where h, k, and l represent Miller planes. The volume of unit cell *V* can be estimated using the expression (3), given the lattice parameters.

$$V = a^2 c \quad (3)$$

As the dosage of Co increased from 0.5 to 3 mol%, the average crystallite size progressively declined. However, with a further rise in Co dosage (5 mol%), the average crystallite size increased to 11.3 nm. The primary reason for the reduction in size observed at the lower concentrations of Co is due to the inhibition behaviour of Co^{2+} ions, where the Co^{2+} ions are predominantly located in the grain boundary region and have the potential to prevent the crystal growth during the hydrothermal treatment [5]. On the contrary, at higher Co dosage, the distribution of dopants on the surface becomes inhomogeneous (surface segregation) [13], leading to the enlargement of crystallite size [14]. A small change in lattice parameters (a and c) and volume of unit cell is expected from the incorporation of Co into the structure of SnO_2 [15].

Table 1 The crystallographic parameters calculated from XRD data.

Samples	Crystallite size (nm)	Lattice parameter, a (Å)	Lattice parameter, c (Å)	Volume of unit cell (Å)
SnO_2	25.0	4.730	3.175	71.38
0.5Co:SnO_2	13.2	4.740	3.178	71.40
1Co:SnO_2	10.1	4.742	3.177	71.43
3Co:SnO_2	8.3	4.749	3.178	71.67
5Co:SnO_2	11.3	4.755	3.178	71.85

3.1.2 UV-Vis

The optical properties of SnO_2 nanorods were studied using a UV-Vis spectrometer. Figure 2 shows the UV–Vis absorption spectra of undoped SnO_2 and 5Co:SnO_2 samples. The UV-Vis absorption data was used to calculate the band gap energy by plotting a graph of $(\alpha h\nu)_2$ versus photon energy, $h\nu$. The band gap energy of the samples can be estimated from the intercept of the linear portion of the plot, as shown in the inset of Figure 2. As depicted in Figure 2, both samples exhibit a prominent absorption peak in the UV-Vis region, with a noticeable red shift observed in the absorption edge for 5Co:SnO_2. Notably, an additional peak was observed in 5Co:SnO2 near the visible light region, potentially resulting from an increase in defect sites in the lattice structure of SnO_2 due to the substitution of Co^{2+} ions. This peak may be attributed to the charge-transfer transitions from the valence to the conduction band of SnO_2 [16]. The calculated band gap of undoped SnO_2 (3.87 eV) is slightly greater than that of bulk SnO_2 (3.62 eV). This variation is due to the smaller particle size (~25 nm) compared to bulk SnO_2. This finding parallels to the earlier report [11]. In the case of 5Co:SnO_2, incorporating Co dopant reduced the band gap to 3.79 eV. This can be elucidated by the interaction of *d* electrons in the Co dopant and conduction band of SnO_2, causing a shift in fermi level, resulting in the band gap narrowing [17].Consequently, the electron concentration within the conduction band increases, thereby enhancing the efficacy of the interfacial charge transfer process during the gas sensing test [18, 19] .

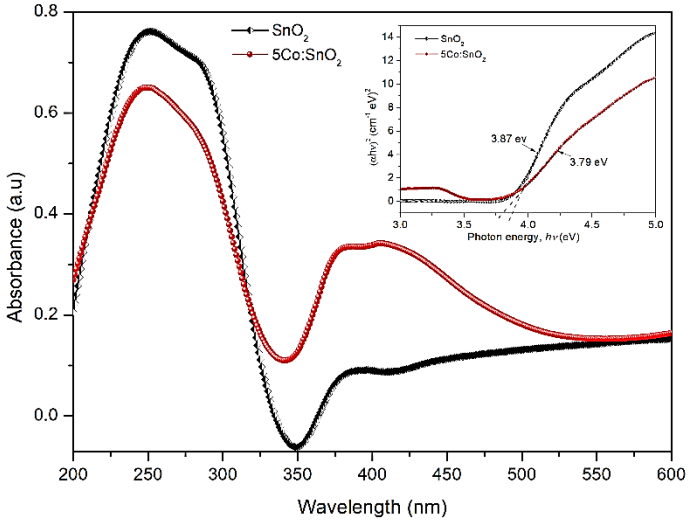

Figure 2 UV-Vis spectra and band gap calculation (inset) for undoped SnO_2 and 5Co:SnO_2 nanorods.

3.1.3 HRTEM/SAED

Further study on crystal structure was carried out using HRTEM/SAED analysis. Figure 3 shows the HRTEM images of SnO_2 and 5Co:SnO_2 samples with corresponding SAED patterns. From the images, it is evident that the rod shape remained unchanged even after the doping process. However, there was a noticeable reduction in the average diameter of nanorods in the 5Co:SnO_2 sample. Both samples, undoped SnO_2 and 5Co:SnO_2, show well-crystalline spear-shaped nanorods with an average diameter of ~25 nm and ~14 nm, respectively. The nanorods formed in SnO_2 have a lower degree of agglomeration in comparison to those observed in 5Co:SnO_2. In principle, as the size of the nanoparticle decreases, the particles tend to agglomerate in order to minimize the surface energy [20]. The lattice fringes for SnO_2 were measured to be 0.33 nm and 0.26 nm, corresponding to (110) and (101) planes of rutile tetragonal structure. The marked lattice spacing for 5Co:SnO_2 is found to be 0.33 nm, associated with (110) plane of rutile tetragonal SnO_2. The SAED patterns recorded for SnO_2 and 5Co:SnO_2 are shown in the insets of Figures 3 (b) and 3(d), which explain the polycrystalline nature of the samples. The diffraction rings are indexed as (110), (101), (200) and (211), further confirming the rutile tetragonal samples [4]. The findings agree with the XRD patterns, which identified the (110) (101) and (211) planes as the most prominent peaks for both samples.

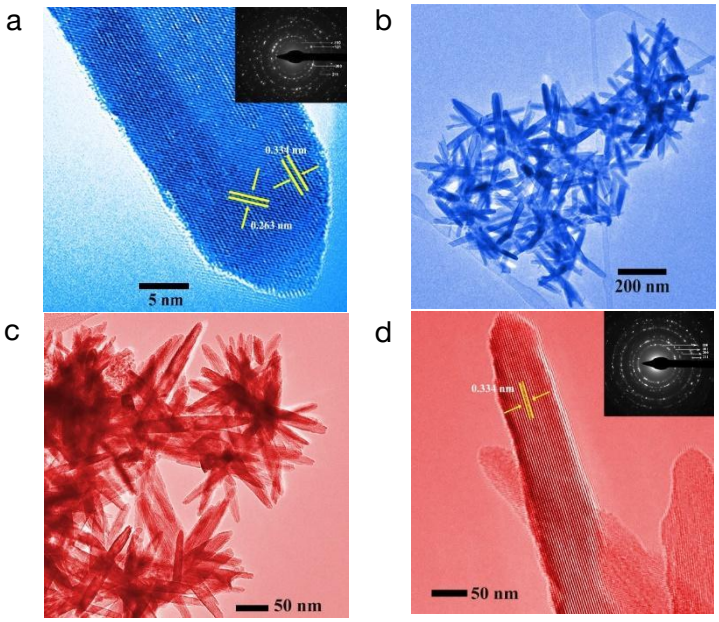

Figure 3 HRTEM images of (a) and (c) low magnification images of SnO_2 (38 Kx) and 5Co:SnO_2 (97 Kx), respectively. (b) and (d) high magnification of SnO_2 (1.05 Mx) and 5Co:SnO_2 (690 Kx) with corresponding SAED patterns (inset).

3.1.4 XPS

The surface composition of the samples was investigated using X-ray photoelectron spectroscopy (XPS). Figure 4 presents the high-resolution XPS spectra of Sn 3d, O 1s and Co 2p for 5Co:SnO_2 sample. The deconvoluted XPS core level Sn 3d spectra of 5Co:SnO_2 show the presence of Sn with two different oxidation states (Figure 4(a). The main peaks can be associated with Sn^{4+} $3d_{3/2}$ (495.1 eV) and Sn^{4+} $3d_{5/2}$ (486.8 eV), respectively [10, 21]. Additionally, the presence of double peaks at binding energies of 492.9 eV and 485.2 eV can be attributed to Sn^{2+} $3d_{3/2}$ and Sn^{2+} $3d_{5/2}$, respectively [11].

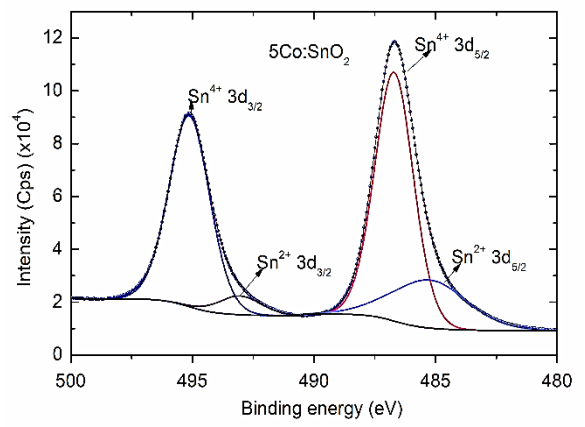

(a)

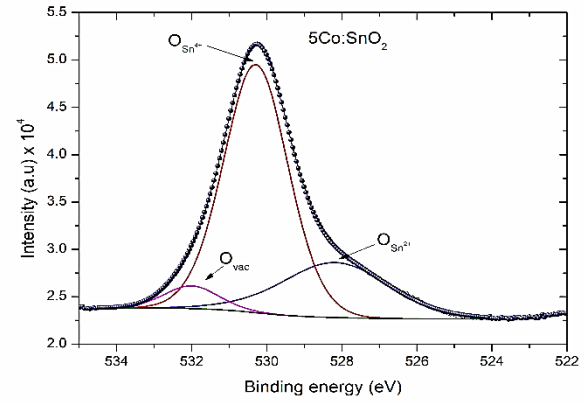

(b)

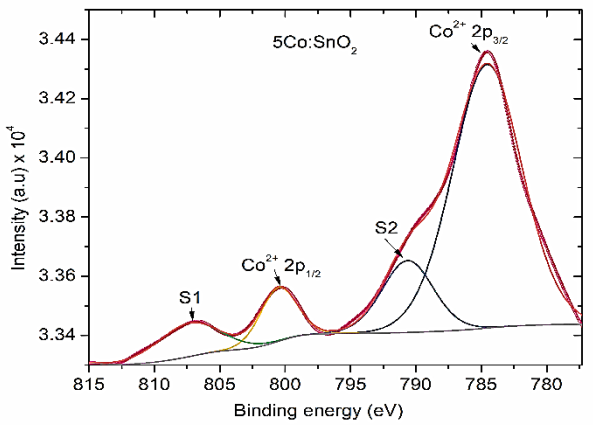

(c)

Figure 4 The XPS spectra of 5Co:SnO_2**:** (a) Sn 3d, (b) O 1s and (c) Co 3p .

Meanwhile, the deconvolution of the O (1s) peaks shows three Gaussian peaks, as shown in Figure 4(b). The primary peak, located at the binding energy of 530.3 eV can be attributed to the lattice oxygen with the chemical state Sn^{4+} (SnO_2) [22] Meanwhile, the peak at lower binding energy (528.1 eV) corresponds to the lattice oxygen of SnO. The appearance of a third peak at a higher binding energy (531.9 eV) has been related to either the chemisorbed oxygen species such as hydroxide (-OH) or can be associated with the presence of oxygen vacancies, O_{vac} [23]. This peak is expected in 5Co:SnO_2 as doping with Co^{2+} ions substituting Sn^{4+} ions must have initiated the creation of O_{vac} defects in SnO_2 lattice [11]. Figure 4(c) shows the Co 2p spectrum of 5Co:SnO_2. There are peaks of Co $2p_{1/2}$ and Co $2p_{3/2}$ at the binding energies of 800.7 eV and 784.9 eV, respectively, along with two satellite peaks which resulted from Co^{2+}. The binding energy difference between the two Co 2p peaks is recorded as 15.8 eV, which indicates the absence of other cobalt clusters [24].

3.2 Ethanol Gas Sensing Test

The ethanol gas sensing test was carried out to compare the performance of SnO_2 sensor material before and after doping. Figure 5 presents the sensing response of SnO_2 and 5Co:SnO_2 towards 1000 ppm C_2H_5OH/N_2 gas. The sensor response increased from 1.1 x 10^3 to 3.3 x 10^3, indicating a sensitivity approximately three times higher than undoped SnO_2. Although the response time taken by both samples was 60 seconds, 5Co:SnO_2 exhibited better recovery than SnO_2.

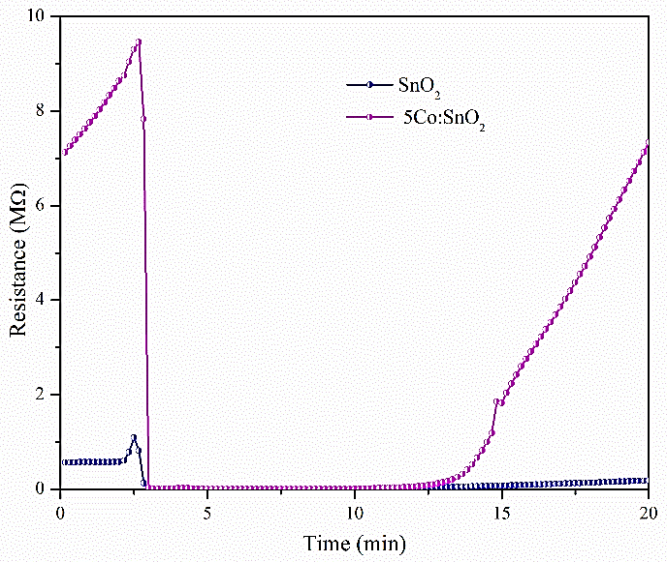

Figure 5 The ethanol sensing response of SnO_2 and 5Co:SnO_2 at 450℃.

In the initial stage of the ethanol sensing test, the oxygen molecules from the surrounding environment adsorb on the surface of the SnO_2 and 5Co:SnO_2, and then, trapping the electrons from the conduction band of the sensor material. As the sensor operates at 450°C, the oxygen molecules undergo ionization, mostly forming O^{2-} (ads). The observed increase in the initial resistance of the 5Co:SnO_2 sensor can be attributed to the reduction in bandgap energy. This reduction facilitates the oxygen molecules adsorbed on the sensor surface to capture electrons more effectively from the conduction band. Consequently, the electron depletion layer experiences an increase in thickness, leading to a significant rise in the initial resistance of 5Co:SnO_2 in comparison to SnO_2 [25].

$$O_2\,(gas) \;\rightarrow\; O_2\,(ads) \qquad (4)$$

$$O_2(ads) + 4e \;\rightarrow\; 2O^{2-}\,(ads) \quad (T \geq 400\,℃) \qquad (5)$$

Upon introducing ethanol gas, the molecules reacted with chemisorbed oxygen species, O^{2-} (ads), present on the sensor surface and released electrons back. Consequently, this causes a narrowing of the electron depletion layer, decreasing the resistance value. The corresponding reaction is shown in equation (4) and (5) [5].

$$C_2H_5OH\,(ads) + 6O^{2-}(ads) \;\rightarrow\; 2CO_2\,(gas) + 3H_2O\,(gas) + 2e \qquad (6)$$

Based on the physiochemical characterization, the gas sensing performance of the 5Co:SnO_2 towards ethanol gas in this study can be attributed to the smaller size of the nanorod, which increases the surface area, thereby a greater number of

catalytically active sites available for adsorption. In addition, both the existence of oxygen vacancies [26, 27] and band gap narrowing may further facilitate the charge transfer between ethanol gas and the sensor surface [18, 19].

4.0 CONCLUSION

In summary, cobalt doped SnO_2 nanorods has been successfully produced *via* a simple hydrothermal method. The findings indicate that incorporating Co into SnO_2 crystal lattice led to changes in physicochemical properties, particularly band gap reduction, particle size reduction and the formation of oxygen vacancies. The ethanol gas sensing test was conducted on both SnO_2 and 5Co:SnO_2 samples at 450°C. The results demonstrated that the ethanol sensing response significantly improved after doping with Co. Thus, the Co-doped SnO_2 nanorods exhibit significant potential as a viable material for ethanol sensors in applications requiring higher operating temperatures.

Acknowledgment

The authors gratefully acknowledge Prof. Dr. As. Md. Abdul Haseeb and Dr. M.M. Arafat for assisting in the ethanol gas sensing test.

References

[1] Seiyama, T., Kato, A., Fujiishi, K., and Nagatani, M. 1962. A new detector for gaseous components using semiconductive thin films. *Analytical Chemistry,* 34(11), 1502-1503.

[2] Goel, N., Kunal, K., Kushwaha, A., and Kumar, M. 2023. Metal oxide semiconductors for gas sensing. *Engineering Reports,* 5(6), e12604.

[3] Pandit, N. A. and Ahmad, T. 2022. Tin oxide based hybrid nanostructures for efficient gas sensing. *Molecules,* 27(20), 7038.

[4] Jahnavi, V. S., Tripathy, S. K., and Ramalingeswara Rao, A. V. N. 2019. Structural, optical, magnetic and dielectric studies of SnO_2 nano particles in real time applications. *Physica B: Condensed Matter,* 565(61-72).

[5] Tan, Y. and Zhang, J. 2023. Highly sensitive ethanol gas sensors based on Co-doped SnO_2 nanobelts and pure SnO_2 nanobelts. *Physica E: Low-dimensional Systems and Nanostructures,* 147, 115604).

[6] Patil, A. S., Patil, A. V., Dighavkar, C. G., Adole, V. A., and Tupe, U. J. 2022. Synthesis techniques and applications of rare earth metal oxides semiconductors: A review. *Chemical Physics Letters,* 796, 139555.

[7] Shi, J., Quan, W., Chen, X., Chen, X., Zhang, Y., Lv, W., Yang, J., Zeng, M., Wei, H., and Hu, N. 2021. Noble metal (Ag, Au, Pd and Pt) doped TaS_2 monolayer for gas sensing: A first-principles investigation. *Physical Chemistry Chemical Physics,* 23(34), 18359-18368.

[8] Ni, J., Quintana, M., and Song, S. 2020. Adsorption of small gas molecules on transition metal (Fe, Ni and Co, Cu) doped graphene: A systematic DFT study. *Physica E: Low-dimensional Systems and Nanostructures,* 116, 113768.

[9] Ojha, B., Aleksandrova, M., Schwotzer, M., Franzreb, M., and Kohler, H. 2023. Thermo-cyclically operated metal oxide gas sensor arrays for analysis of dissolved volatile organic compounds in fermentation processes: Part I–Morphology aspects of the sensing behavior. *Sensing and Bio-Sensing Research,* 40100558.

[10] Inderan, V., Arafat, M., Kumar, S., Haseeb, A., Jiang, Z.-T., Altarawneh, M., and Lee, H. L. 2017. Study of structural properties and defects of Ni-doped SnO_2 nanorods as ethanol gas sensors. *Nanotechnology,* 28(26), 265702.

[11] Ali, S. I., Dutta, D., Das, A., Mandal, S., and Mandal, A. C. 2023. Understanding the structure-property correlation of tin oxide nanoparticles synthesized through the sol-gel technique. *Journal of Luminescence,* 253, 119465.

[12] Naz, S., Javid, I., Konwar, S., Surana, K., Singh, P. K., Sahni, M., and Bhattacharya, B. 2020. A simple low cost method for synthesis of SnO_2 nanoparticles and its characterization. *SN Applied Sciences,* 2, 1-8.

[13] Aragón, F., Coaquira, J. A. H., Gonzalez, I., Nagamine, L., Macedo, W., and Morais, P. 2016. Fe doping effect on the structural, magnetic and surface properties of SnO_2 nanoparticles prepared by a polymer precursor method. *Journal of Physics D: Applied Physics,* 49(15), 155002.

[14] Tan, L., Wang, L., and Wang, Y. 2011. Hydrothermal synthesis of SnO_2 nanostructures with different morphologies and their optical properties. *Journal of Nanomaterials,* 2011, 1-10.

[15] Vomáčka, P., Štengl, V., Henych, J., and Kormunda, M. 2016. Shape-controlled synthesis of Sn-doped CuO nanoparticles for catalytic degradation of Rhodamine B. *Journal of colloid and interface science,* 481, 28-38.

[16] Cai, X., Cai, Y., Liu, Y., Li, H., Zhang, F., and Wang, Y. 2013. Structural and photocatalytic properties of nickel-doped zinc oxide powders with variable dopant contents. *Journal of Physics and Chemistry of Solids,* 74(9), 1196-1203.

[17] Ahuja, P., Ujjain, S. K., Kanojia, R., and Attri, P. 2021. Transition metal oxides and their composites for photocatalytic dye degradation. *Journal of Composites Science,* 5(3), 82.

[18] Gao, M., Zhu, L., Peh, C. K., and Ho, G. W. 2019. Solar absorber material and system designs for photothermal water vaporization towards clean water and energy production. *Energy & Environmental Science,* 12(3), 841-864.

[19] Sun, Y., Fu, S., Sun, S., Cui, J., Luo, Z., Lei, Z., and Hou, Y. November 7, 2023. Design of a SnO_2/zeolite gas sensor to enhance formaldehyde sensing properties: from the strategy of the band gap-tunable zeolite. *ACS Applied Materials & Interfaces,* 15(46), doi: 10.1021/acsami.3c12789.

[20] Keskinen, H., Tricoli, A., Marjamäki, M., Mäkelä, J. M., and Pratsinis, S. E. 2009. Size-selected agglomerates of SnO_2 nanoparticles as gas sensors. *Journal of Applied Physics,* 106(8).

[21] Inderan, V., Arafat, M., Haseeb, A., Sudesh, K., and Lee, H. L. 2019. A Comparative Study of Structural and Ethanol Gas Sensing Properties of Pure, Nickel and Palladium Doped SnO_2 Nanorods Synthesised by the Hydrothermal Method. *Journal of Physical Science,* 30(1).

[22] Huang, J., Wang, L., Gu, C., Zhai, M., and Liu, J. 2013. Preparation of hollow porous Co-doped SnO_2 microcubes and their enhanced gas sensing property. *CrystEngComm,* 15(37), 7515-7521.

[23] Hsieh, P. T., Chen, Y. C., Kao, K. S., and Wang, C. M. 2008. Luminescence mechanism of ZnO thin film investigated by XPS measurement. *Applied Physics A: Materials Science and Processing,* 90(2), 317-321,

[24] Ehsan, M. A., Hakeem, A. S., and Rehman, A. 2020. Hierarchical growth of CoO nanoflower thin films influencing the electrocatalytic oxygen evolution reaction. *Electrocatalysis,* 11, 282-291.

[25] Kou, X., Xie, N., Chen, F., Wang, T., Guo, L., Wang, C., Wang, Q., Ma, J., Sun, Y., Zhang, H., and Lu, G. 2018. Superior acetone gas sensor based on electrospun SnO_2 nanofibers by Rh doping. *Sensors and Actuators B: Chemical,* 256, 861-869.

[26] Sun, Y., Hou, T., Sun, S., Du, H., Fu, S., and Wang, J. 2022. Synergistic effects of zeolite and oxygen vacancies in SnO_2 for formaldehyde sensing: Molecular simulation insights & experimental verification. *Applied Surface Science,* 604, 154511.

[27] Zhou, J. Y., Bai, J. L., Zhao, H., Yang, Z. Y., Gu, X. Y., Huang, B. Y., Zhao, C. H., Cairang, L., Sun, G. Z., and Zhang, Z. X. 2018. Gas sensing enhancing mechanism via doping-induced oxygen vacancies for gas sensors based on indium tin oxide nanotubes. *Sensors and Actuators B: Chemical,* 265, 273-284.